Research Article Vol. 33, No. 22 / 3 Nov 2025 / Optics Express 45949
Optics EXPRESS

XPCIpy: A Python toolkit for X-ray phase-contrast imaging

VICTOR SANCHEZ-LARA* AND DIEGO GARCIA-PINTO

Universidad Complutense de Madrid, Madrid, 28040, Spain
*vicsan05@ucm.es

Abstract: X-ray absorption-based imaging often yields insufficient contrast for materials with low atomic numbers. X-ray phase-contrast imaging (PCI) offers a solution by leveraging the phase shift induced by different materials, enabling enhanced visualization of structures with minimal absorption differences. However, extracting phase information from intensity measurements is a non-trivial task, requiring specialized techniques. We present XPCIpy, an open-source software developed in Python, designed for both the simulation of X-ray PCI, including propagation-based imaging (PBI) and Talbot-Lau phase-contrast Imaging (TLPCI), and the reconstruction of TLPCI images. XPCIpy implements the phase stepping method for image retrieval, offering both least-squares and fast Fourier transform (FFT)-based reconstruction algorithms. It notably includes an algorithm for correcting phase step and dose fluctuations, which helps mitigate reconstruction artifacts like Moiré patterns. The software's modular architecture enhances extensibility, and a user-friendly graphical user interface (GUI) improves accessibility for researchers. Validated through both simulations and experimental data, XPCIpy provides a versatile framework to optimize experimental setups, test new reconstruction algorithms, and serve as an accessible tool for the scientific community in X-ray phase-contrast imaging. The code is publicly available at https://github.com/PREDICO-Project/XPCIpy.

1. Introduction

X-ray absorption-based imaging is a widely used technique in medical imaging. The contrast in these images arises from the differential attenuation of X-rays as they interact with matter. However, when different materials exhibit similar attenuation properties, the resulting contrast is often insufficient, limiting the ability to distinguish them. X-ray Phase-Contrast Imaging (PCI) [1] has emerged as a solution to address the limitations of weak contrast in conventional X-ray imaging. This approach leverages the contrast arising from the phase shift induced by different materials, rather than relying on absorption-based contrast used in traditional X-ray imaging. Unlike attenuation, phase contrast is sensitive to variations in the refractive index, enabling enhanced visualization of structures with minimal absorption differences [2]. It has been used to characterize density differences in composite materials [3], enabling the detection of internal structures or defects with improved contrast. In the biomedical field, phase contrast techniques are being explored for applications such as mammography [4,5], where they have the potential to improve lesion detectability. Moreover, recent studies have evaluated its utility in lung cancer diagnosis [6], assessing whether phase contrast X-ray imaging can provide better tumour visualisation and diagnostic accuracy compared to standard imaging modalities.

However, extracting phase information from intensity measurements is inherently non-trivial. All phase-contrast techniques require dedicated reconstruction algorithms [7–10]. In addition, some techniques like grating-based interferometry also require specialized equipment, including micrometric gratings [11].

Propagation-based Imaging (PBI) [12,13], also known as in-line PCI, is one of the most commonly used techniques to obtain phase-contrast images. In this method, the contrast arises from the propagation of X-rays through the object of interest [14]. If the propagation distance

#573918 https://doi.org/10.1364/OE.573918
Journal © 2025 Received 17 Jul 2025; revised 16 Sep 2025; accepted 16 Sep 2025; published 21 Oct 2025

Optics EXPRESS

is sufficiently large, a phenomenon known as edge enhancement occurs [15], where phase discontinuities at the boundary of the object result in additional contrast in the image. This enhanced contrast is due to the phase shift imparted to the X-rays as they pass through the object, which can highlight features that are not easily visible in absorption-based images [16]. Various algorithms are available to retrieve phase information from these edge-enhanced images. Among the most widely used are phase retrieval methods based on the transport of intensity equation (TIE) [12]. Since TIE-based methods are applicable only to PBI, alternative approaches are needed for other phase contrast techniques, as will be discussed later in this work. One of the main limitations of PBI is that it requires spatially coherent and monoenergetic X-ray beams, conditions that can only be achieved with the use of synchrotron radiation sources [17] or micro-focus X-ray sources [18]. Despite this limitation, PBI offers high spatial resolution in the obtained phase-contrast images and does not require additional specialized equipment beyond the X-ray source and detector setup. This simplicity in implementation, combined with its high resolution, makes PBI an attractive option for studies requiring fine structural detail [5,19].

To reduce the stringent requirements on spatial coherence, different techniques that allow PCI have been developed, such as speckle-based imaging (SBI) [20,21] or grating-based imaging (GBI) [11,22]. They are based on the diffraction produced by the gratings or a speckle pattern object to enhance phase effects in the intensity recorded in the detector.

GBI can be utilized with micro-focus and conventional X-ray tubes, allowing for the simultaneous acquisition of multiple images of the sample, each providing distinct information about its characteristics. These images are attenuation, phase gradient, and dark-field images, which are obtained through the application of specialized reconstruction algorithms [23]. Talbot-Lau phase-contrast imaging (TLPCI) is a specific implementation of GBI techniques, which employs three gratings to enable phase contrast imaging with conventional X-ray sources [24].

Although the GBI technique is one of the most effective PCI methods [25], its primary limitation lies in the high cost of constructing the gratings, which must be specifically designed for each experimental setup [26]. Additionally, artifacts may arise in the reconstruction process as a result of misalignment of the gratings [27], as well as from inaccuracies due to mechanical limitations. The gratings must be moved during the image acquisition and their relative position must be precise. In practice, there will be deviations in the position, producing artifacts in the phase contrast images.

Therefore, it is essential to have tools that enable both the simulation of GBI systems and the implementation of robust reconstruction algorithms. To this end, the software presented in this work includes an algorithm for correcting grating position errors, improving the reconstructed images [28].

While the fields of X-ray phase-contrast simulation and phase retrieval are well-established, with various specialized tools and algorithms described in the literature, there remains a gap for an unified, open-source framework that combines comprehensive simulation capabilities with robust reconstruction methods. This work addresses this need by introducing XPCIpy, a novel Python toolkit that consolidates a wide range of functionalities into a single and accessible platform. XPCIpy not only provides a unified simulation framework for both PBI and TLPCI, but also implements algorithms to reconstruct TLPCI images, a key module of the framework, and generates synthetic datasets with well-known Moiré artifacts. Thanks to its modular architecture and user-friendly graphical user interface (GUI), XPCIpy offers enhanced accessibility and usability, making it a valuable tool for both research and education.

The remainder of this paper is organized as follows. Section 2, 'Materials and methods,' provides a comprehensive overview of the theoretical framework underlying X-ray phase-contrast imaging and details the architecture and functionalities of the XPCIpy software. This includes a description of the Talbot-Lau interferometer design, the phase stepping method employed for image acquisition and retrieval, and an in-depth look at the individual modules within the

Optics EXPRESS

XPCIpy environment. In Section 3, 'Results,' we present the validation of XPCIpy through both simulations, showcasing its capabilities in modeling PBI and TLPCI, and experimental data obtained from a laboratory setup. Finally, Section 4 offers a discussion of the software's broader implications and its potential for future enhancements, while Section 5 concludes the paper by summarizing its key contributions.

2. Materials and methods

The complex refractive index of a material can be described as shown in Eq. (1). The real part of the refractive index is related to the phase shift introduced on the X-ray beam, and the imaginary part is related to the attenuation.

$$n = 1 - \delta + i\beta. \tag{1}$$

An object can be described by its transmission function, which contains all the information related to the interaction with the X-ray wave function.

$$O(x, y) = \exp\left[-\mu(x, y) + i\Phi(x, y)\right]. \tag{2}$$

The real part is the attenuation of the transmission function and it can be written as:

$$\mu(x, y) = \frac{2\pi}{\lambda} \int \beta(x, y, z)\, dl. \tag{3}$$

The λ parameter is the wavelength of the x-ray beam and the integral is the line integral of the imaginary part of the complex refractive index (Eq. (1)). Analogously, a similar equation can be derived to relate $\Phi(x, y)$ and the real term of the refractive index [29].

$$\Phi(x, y) = -\frac{2\pi}{\lambda} \int \delta(x, y, z)\, dl. \tag{4}$$

To retrieve the information related to the attenuation and phase introduced by the object, a Talbot-Lau interferometer is used, which is composed of three gratings.

2.1. Talbot Lau interferometer

A Talbot-Lau interferometer, as depicted in Fig. 1, employs three gratings (G0, G1, and G2) aligned along the optical axis to enable phase-contrast imaging. G0, the source grating, generates a set of spatially coherent X-ray sources, ensuring the necessary coherence for phase effects. Its period (p_0) is chosen based on the system geometry:

$$p_0 = \frac{z_{01}}{z_{12}} p_2, \tag{5}$$

where z_{01} is the distance between G0 and G1 and z_{12} the distance between G1 and G2, with p_2 being the period of G2. G1, the phase grating, introduces a known phase shift(π or $\pi/2$) to the X-ray beam, with the object typically positioned immediately before or after it for maximized sensitivity. The interferometer operates on the principle of the fractional Talbot effect [30], where self-images of a periodic object are formed at specific distances D_{fT}:

$$D_{fT} = \frac{m}{2\lambda}\left(\frac{p}{\eta}\right)^2 = \frac{m}{4\eta^2} D_T \quad m = 1, 3, 5 \cdots \tag{6}$$

Here, η is a parameter dependent on the phase shift introduced by the grating ($\eta = 1$ for $\pi/2$ and $\eta = 2$ for π), and D_T is the Talbot distance for an absorption grating. The self-image periodicity is given by $p' = p/\eta$. Figure 2 illustrates the Talbot effect for a phase grating, showing how the pattern is modified by a sample.

G2, the analyzer grating, is an absorption grating placed at a fractional Talbot distance of G1's self-image and with matching periodicity. By displacing G1 or G2 perpendicularly to their bars, the detected intensity varies, which is essential for the phase stepping method.

Optics EXPRESS

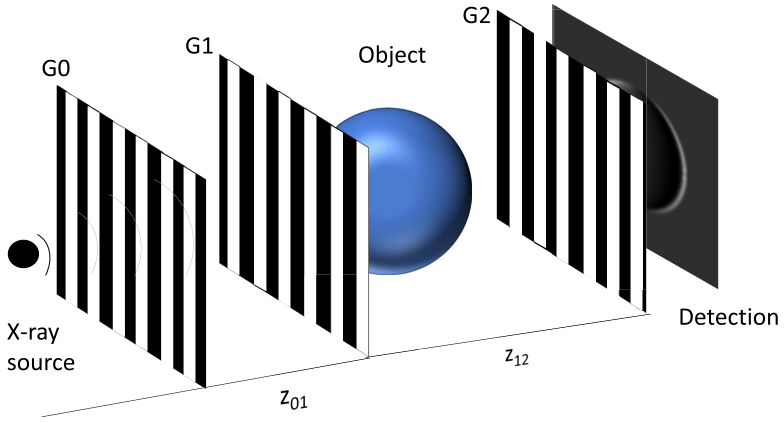

Fig. 1. Talbot-Lau interferometer setup.

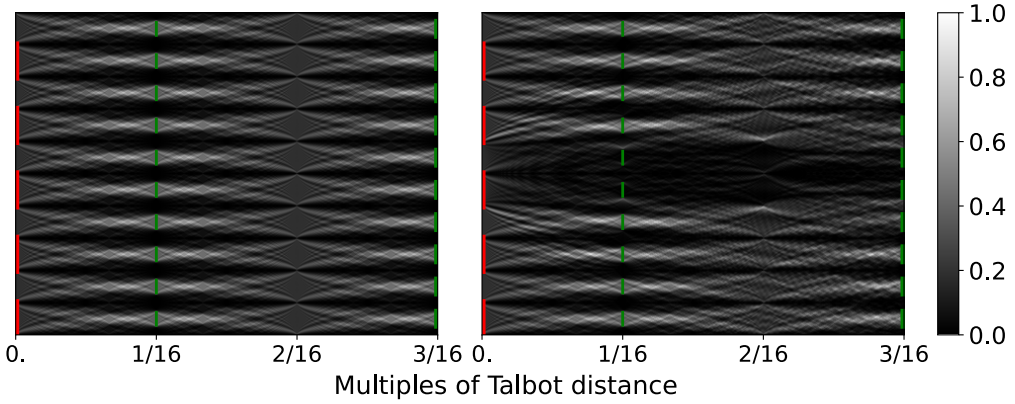

Fig. 2. Talbot effect for a π phase grating. At 1/16 and 3/16 multiples of Talbot distance, the self-image of the grating is formed. Red lines indicates the bars of the phase grating, green lines indicates the self-image. (a) Talbot effect without object, (b) Talbot effect with an object after the phase grating.

2.2. *Phase retrieval methods*

Retrieving phase information from X-ray intensity measurements is an inverse problem, and various techniques have been developed to address it. While novel approaches, including those based on deep neural networks [31,32] and Moiré pattern reconstruction [33], offer advanced solutions, analytical methods often require specific acquisition schemes. For grating-based phase contrast imaging, obtaining the full phase information typically necessitates multiple intensity measurements.

The phase stepping method [34] is a widely used analytical approach for phase retrieval. This technique relies on acquiring multiple images by incrementally displacing a grating (G1 or G2 in a Talbot-Lau interferometer) perpendicularly to the optical axis. In an ideal system, the intensity for each pixel across these displacements follows a triangular function. However, due to experimental imperfections, the measured intensity modulation curve often approximates a sinusoidal function. For each pixel i and phase step j, the intensity (I_j^i) is described by:

$$I_j^i = o^i + A^i \sin\left(2\pi \frac{x_j}{p_2} + p^i\right). \tag{7}$$

Optics EXPRESS

Here, x_j is the relative position of the gratings, p_2 is G2's period, and o^i, A^i, and p^i represent the offset, amplitude and phase shift of the modulation curve, respectively. These parameters can be extracted from experimental data using least squares fitting or fast Fourier transform (FFT). The intensity of the frequency 0 in the FFT corresponds to the offset (o^i), while the module (A^i) and phase (p^i) of the intensity modulation curve are derived from the first harmonic's complex values. Specifically, if a and b are the real and imaginary parts of the first harmonic:

$$p = \arctan\frac{b}{a}; \tag{8}$$

$$A = 2\sqrt{a^2 + b^2}. \tag{9}$$

To isolate the object's specific contribution to attenuation, ultra-small scattering, and phase shift, the intensity modulation curve with the object (o) is compared to a reference curve (r) obtained without the object (Fig. 3). This comparison yields three distinct images: attenuation (At), phase gradient (PG), and dark field (DF) [23]:

$$\begin{aligned} PG^i &= p_o^i - p_r^i; \\ At^i &= \frac{o_o^i}{o_r^i}; \\ DF^i &= \frac{v_o^i}{v_r^i}, \end{aligned} \tag{10}$$

where visibility v^i is defined as:

$$v^i = \frac{A^i}{o^i}. \tag{11}$$

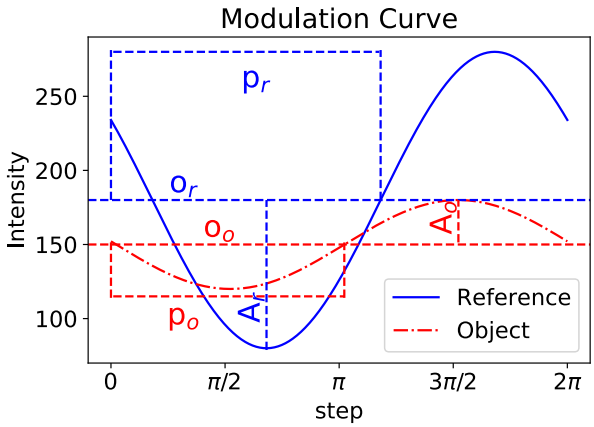

Fig. 3. Intensity modulation curves with an object (red dashed line) and without the object (blue continue line). It is represented the parameters of the sine: the offset (o), the module (A) and the phase (p).

2.3. XPCIpy environment

XPCIpy (X-ray phase-contrast imaging in Python) is an open-source software developed in Python, designed for the simulation of X-ray phase-contrast images (PBI and TLPCI) and the reconstruction of TLPCI images using the phase stepping method. Its modular architecture facilitates easy modification and the integration of new functionalities. The code leverages

Optics EXPRESS

common Python libraries such as NumPy and SciPy, and utilizes Numba for algorithm acceleration. Future developments aim to incorporate GPU acceleration via libraries like Cupy. The XPCIpy environment comprises three main modules, each with specific tasks as detailed in Table 1. Examples of usage, including Jupyter Notebooks, are available in the public GitHub repository [35]:

Table 1. XPCIpy Modules and functionalities

Module	Task
PCSim	Simulation of PBI and TLPCI.
MoireSim	Simple Analytical implementation of equation (7) and Moiré artifacts.
TLRec	Talbot-Lau Reconstruction.

2.3.1. PCSim

The PCSim module simulates PBI and TLPCI by applying Fresnel's Wave Theory of Light to X-rays [14]. The simulation workflow is outlined in Fig. 4.

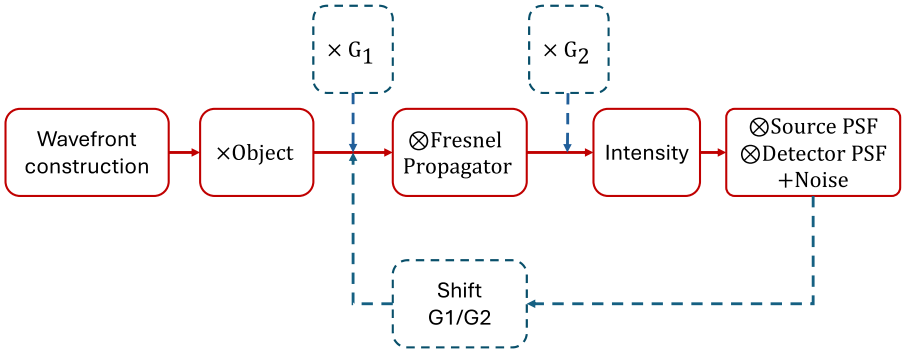

Fig. 4. PCSim workflow. The symbol × denotes the multiplication of transmission functions, while ⊗ denotes the convolution of functions.

The process begins with the geometry and source modules, which define the system configuration and generate the initial wavefront. The geometry module stores the relevant distance. The source module provides the incident wavefront, taking into account its spectrum, source size, and angular distribution.

The next stage involves the object and material modules. The object transmission function $O(x, y)$ is constructed by combining the spatial distribution of the object with the refractive index of the assigned materials (Eq. (2)). For TLPCI simulations, the object list includes the phase grating (G1) and the analyzer grating (G2), whose transmission functions are inserted at the corresponding planes.

Propagation between planes is handled by the propagator module, which applies the Fresnel propagator [29].

The Fresnel number is defined as:

$$N_F = \frac{\Delta x^2}{z\lambda}, \tag{12}$$

where Δx is the pixel size, z is the propagation distance, and λ is the wavelength. When $N_F \ll 1$ the propagation is in the Fraunhofer (far-field) regime, while for $N_F \gtrsim 1$, it is in the Fresnel (near-field) regime. Under the Fresnel regime, the propagated wavefront $U(x, y, z)$ at a distance z

Optics EXPRESS

is calculated via:

$$U(x,y,z) = \mathcal{F}^{-1}\left\{\mathcal{F}\left[O(x,y)\right] \cdot \exp\left[-i\pi\lambda z\left(f_x^2 + f_y^2\right)\right]\right\}, \tag{13}$$

where $O(x,y)$ is the object transmission function, λ is the X-ray wavelength, and f_x and f_y are the spatial frequencies.

At the detector plane, the intensity is obtained as $I(x,y) = |U(x,y,z)|^2$ and convolved by the source point spread function (PSF). The detector module applies the detector response. This includes convolution with the detector PSF, modeled as a Gaussian function to account for blurring introduced by detector resolution. Furthermore, the module allows the downsampling of the image and the inclusion of noise following either Gaussian or Poisson distributions.

For TLPCI simulations, the workflow additionally inserts the transmission functions of the phase grating G1 and the analyzer grating G2 at the appropriate propagation planes. The simulation process is repeated for each relative G1/G2 position required for phase stepping, generating the stack of intensity images that serves as input for the reconstruction module.

The Experiment module provides the control of the simulation pipeline. It allows the user to choose between different experimental configurations. At present, two setups are available: In-line propagation, which models propagation-based phase contrast and phase stepping, which reproduces the acquisition protocol of Talbot-Lau interferometry by shifting the analyzer or the phase grating.

In addition, specific utilities are provided to compute the Talbot carpet for any configuration defined by the user. This functionality allows direct visualization of the self-imaging process generated by a grating at successive propagation distances.

2.3.2. MoireSim

The MoireSim module specializes in simulating Moiré artifacts in TLPCI. This is achieved using the following analytical equation:

$$I_j(x,y) = \exp\left(\lambda_j\right)\left[o(x,y) + A(x,y)\sin\left(2\pi\frac{x_j}{p_2} + \xi_j + p(x,y) + m(x,y)\right)\right], \tag{14}$$

where $I_j(x,y)$ is the intensity at pixel (x,y) for the j-th phase step. In this formulation, $o(x,y)$ represents the sample's attenuation and $p(x,y)$ denotes the phase shift induced by the sample. The term $A(x,y)$ corresponds to the fringe visibility or modulation amplitude. Furthermore, x_j indicates the position of the grating in the j-th phase step, with p_2 being the grating period. The term ξ_j accounts for phase-stepping errors arising from mechanical inaccuracies, and $m(x,y)$ models Moiré patterns resulting from grating misalignments or defects. Finally, λ_j represents dose fluctuations across phase steps, modeled as a multiplicative scaling factor through $\exp(\lambda_j)$. This module also incorporates simple geometrical objects (e.g., spheres, cylinders) as samples for these simulations.

2.3.3. TLRec

This module specifically handles the phase-stepping analysis of TLPCI images for phase-contrast image retrieval. It offers two primary approaches for extracting the intensity modulation curve (Fig. 3): least-squares-based methods and FFT-based methods. Notably, one of the least-squares methods includes an algorithm for correcting estimated phase-step errors, following the approach described by Hashimoto et al. [28], which significantly improves reconstruction accuracy in the presence of mechanical inaccuracies. The workflow of the module is shown in Fig. 5

As input, the module requires two stacks of TIFF images, each stack containing sequential acquisitions corresponding to each phase step (different relative G1-G2 positions). The stacks must be ordered and pre-corrected for detector gain and offset. Once loaded, the code displays

Optics EXPRESS

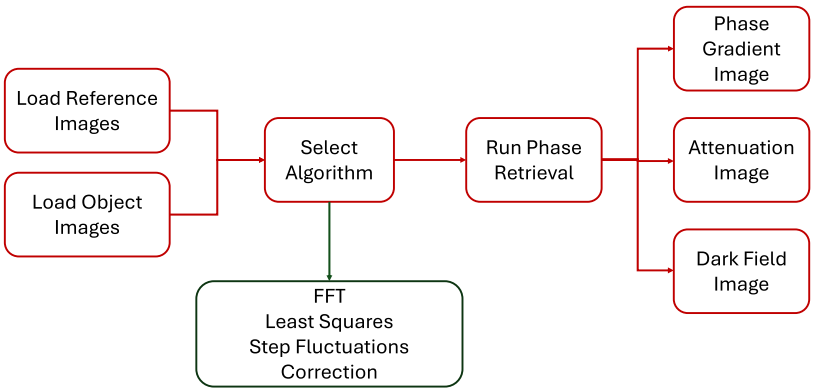

Fig. 5. TLRec module workflow.

the modulation curves obtained from both the reference stack and the object stack for a selected pixel, serving as a verification step to ensure the data have been correctly imported and to confirm that the modulation curves cover at least one period. The user can then select the desired reconstruction algorithm among the available options. Finally, the module produces and displays the three retrieved images, the attenuation, phase gradient and dark-field, and allows exporting the results as TIFF images.

2.3.4. GUI

To enhance user accessibility for non-programmers, a graphical user interface (GUI) has been developed (Fig. 6). The GUI facilitates loading phase-stepping image stacks (object and reference), selecting and executing reconstruction algorithms, displaying results, and saving images. It also includes basic PBI and TLPCI simulation capabilities for simple objects based on Fresnel formalism.

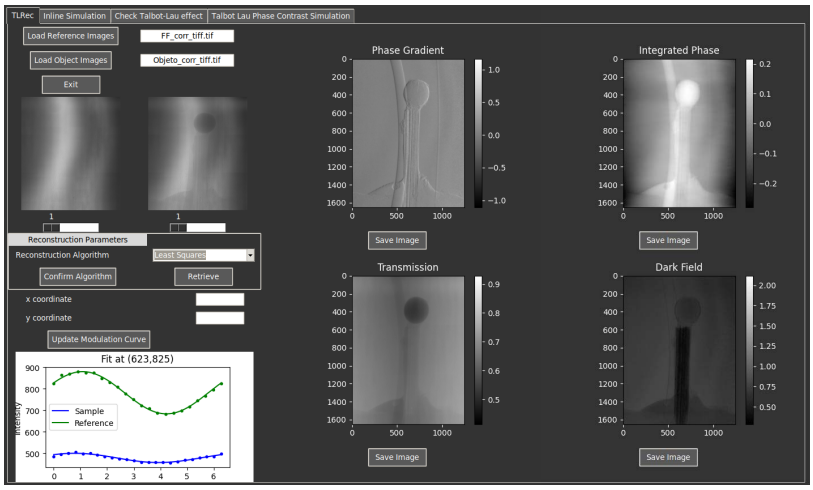

Fig. 6. XPCIpy Graphical User Interface (GUI).

Optics EXPRESS

2.3.5. Technical details and performance

The accuracy and stability of wavefield propagation in XPCIpy are linked to the sampling conditions of the simulation grid. A two-dimensional array of size $N \times N$ with pixel size Δx defines both the field of view (FOV = $N \cdot \Delta x$) and the maximum spatial frequency without aliasing ($f_{Nyquist} = 1/2\Delta x$). In practice, correctly sampling the gratings employed in GBI requires $5-6$ pixels per period to capture the relevant Fourier components of the rectangular shape of the grating. If this condition is not satisfied, the simulation is still performed but a warning appears.

Aliasing can also occur during Fresnel propagation if the sampling condition for Fresnel propagation [36,37] is not fulfilled (Eq. 15).

$$z < N\frac{(\Delta x)^2}{\lambda}, \tag{15}$$

where λ is the wavelength and z the propagation distance. Artifacts may appear if this condition is not met. A strategy to overcome this limitation is to divide the propagation into several shorter steps, each satisfying the condition.

In addition, symmetric padding of the wavefront prior to Fourier propagation can be applied to reduce wrap-around effects at the array boundaries.

Polychromatic simulations are supported by discretizing the source spectrum into N_E energy bins. Each energy is propagated independently and the resulting intensities are combined with weights proportional to the spectral distribution. The computational cost scales linearly with N_E.

Performance benchmarks are illustrated in Fig. 7 for different $N \times N$ grid sizes. As expected, the runtime and memory usage scale with the number of pixels, with Talbot-Lau simulations being more demanding due to the phase-stepping method. The maximum object size that can be simulated is constrained both by the pixel size (which must be small enough to resolve the grating period and to perform the displacement of the grating) and by the available memory.

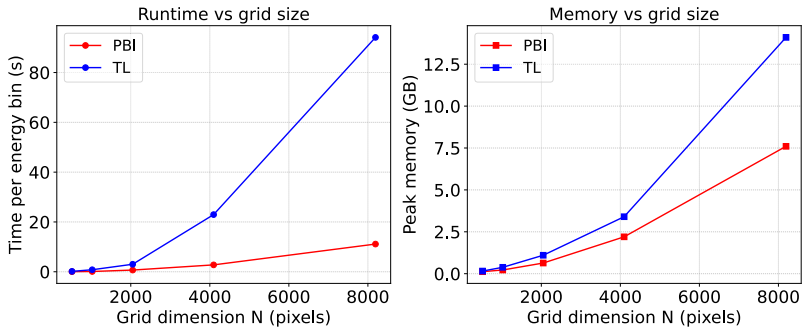

Fig. 7. Performance benchmarks of XPCIpy for typical simulations. The reported values correspond to average runtimes per energy bin (and per phase step in Talbot-Lau simulations) on a HpZ2-Workstation (Intel Core i913900K CPU, 128 GB RAM).

3. Results

The XPCIpy environment supports both phase-contrast image simulation and Talbot-Lau based phase-contrast image reconstruction. The following subsections present key results demonstrating the capabilities of its various modules.

3.1. PCSim

The PCSim module facilitates PCI simulations based on wavefront propagation and interactions with matter, adhering to the workflow detailed in Fig. 4. To evaluate its application for PBI,

Optics EXPRESS

simulations were conducted for both purely absorbing and purely phase shifting spheres. These simulations explored the impact of varying object-detector distances (D) and source diameters (R) on the resulting image intensity. As illustrated in Fig. 8, PBI principles are evident, with edge enhancement (a phase effect) requiring the sample to be positioned at a specific distance from the detector and a small (micrometer-scale) X-ray focal spot. Purely absorbing objects, as expected, do not exhibit this edge enhancement.

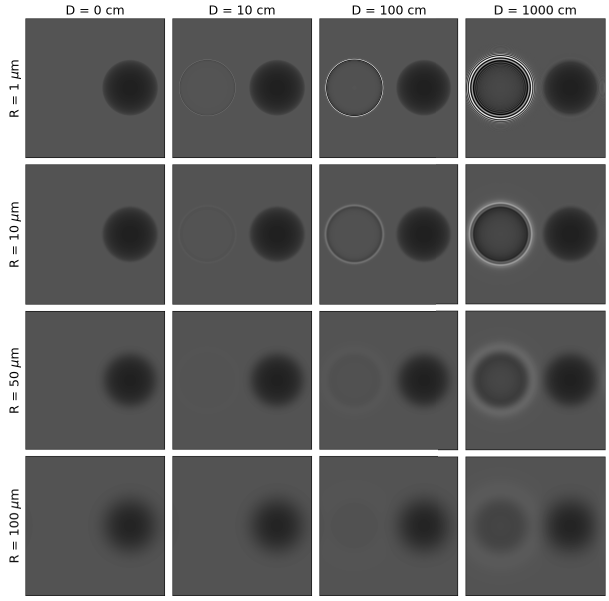

Fig. 8. Simulated PBI images of a pure phase-shifting sphere ($\delta = 4.24 \cdot 10^{-7}$, left) and a pure absorption sphere ($\beta = 4.05 \cdot 10^{-9}$, right), both with a radius of 200 μm. The simulations were performed with a pixel size of 1 μm at an X-ray energy of 25 keV for different object-detector distances (D) and source diameters (R).

Accurate simulation of the Talbot effect is crucial for Talbot-Lau-based phase-contrast imaging (see Section 2.1). PCSim successfully verifies this effect using absorption, π and $\pi/2$ gratings (Fig. 9).

Fig. 9 demonstrates that phase gratings produce self-images at fractional Talbot distances (Eq. (6)), with periodicity conforming to Eq. (7). While the top row illustrates the monochromatic case (design energy of 17.5 keV), the bottom row demonstrates the degradation of visibility under polychromatic illumination, simulated using an X-ray tube spectrum at 30 kVp with a Mo anode and 0.03 mm Mo filtration (Fig. 10).

Once the Talbot effect was correctly integrated, TLPCI simulations were performed. A simulation was performed with a setup involving a calcium sphere (100 μm radius) illuminated by a 23 keV plane wave X-ray source, the pixel size is 0.1 μm. Grating G1 was a $\pi-$phase grating with a 6 μm period and a 0.5 duty cycle, while G2 was an attenuation grating with a 3 μm periodicity. For this configuration, the fractional Talbot distance was 8.35 cm. The phase-stepping process comprised 10 steps, each a 0.3 μm displacement. The simulated phase steps are presented in Fig. 11(a)-(d), and the corresponding Intensity Modulation Curves for reference and object acquisitions are shown in Fig. 11(e).

Optics EXPRESS

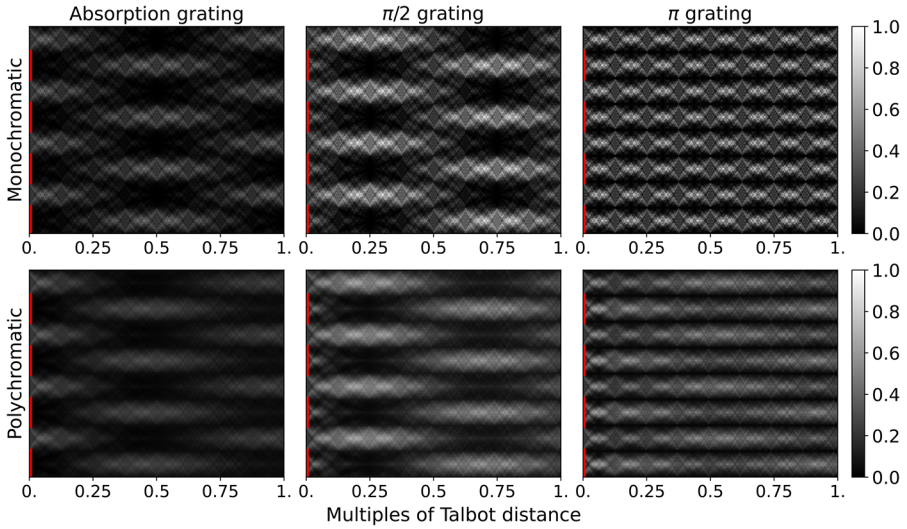

Fig. 9. Simulated Talbot carpets for different grating types: purely absorbing grating, $\pi/2$ grating and π grating, under monochromatic (top row) and polychromatic (bottom row) illumination. All gratings have a period of 100 μm and were simulated with a pixel size of 1 μm over 300 propagation distances. The absorbing grating bars were modeled as 100 μm of gold. Intensities are normalize and red lines indicate the position of the grating bars.

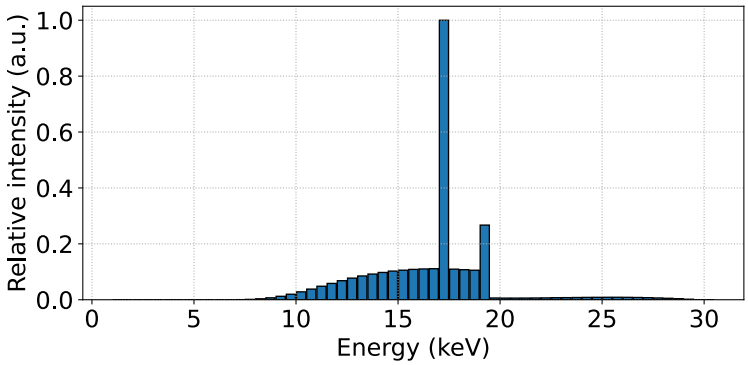

Fig. 10. Discretized spectrum used in the simulation shown in Fig. 9. Corresponds to a 30 kVp Mo-Mo spectrum with a filtration of 0.03 mm.

3.2. *MoireSim*

The MoireSim module's functionality was assessed by simulating a sphere (300 μm radius) with given parameters ($\frac{2\pi}{\lambda}\delta = 10^{-2}\mu m^{-1}$ and $\frac{2\pi}{\lambda}\beta = 10^{-3}\mu m^{-1}$). Moiré fringes, intentionally introduced by a mismatch in G1 and G2 periods (resulting in 6 vertical periods), were analyzed over 20 phase steps.

When the phase stepping method is performed without step or dose fluctuations, Moiré fringes, although visible in raw images, do not appear in the reconstructed PG image (Fig. 12(a)). However, introducing step position fluctuations causes a Moiré pattern with twice the raw image's periodicity to appear in the PG image, accompanied by a slight intensity offset (Fig. 12(b)). The addition of dose fluctuations leads to Moiré fringes in the final PG image with components at both the original Moiré pattern's periodicity and twice that (Fig. 12(c), (d)). In attenuation images, Moiré artifacts generally exhibit very low signal levels and remain imperceptible (Fig. 13).

Optics EXPRESS

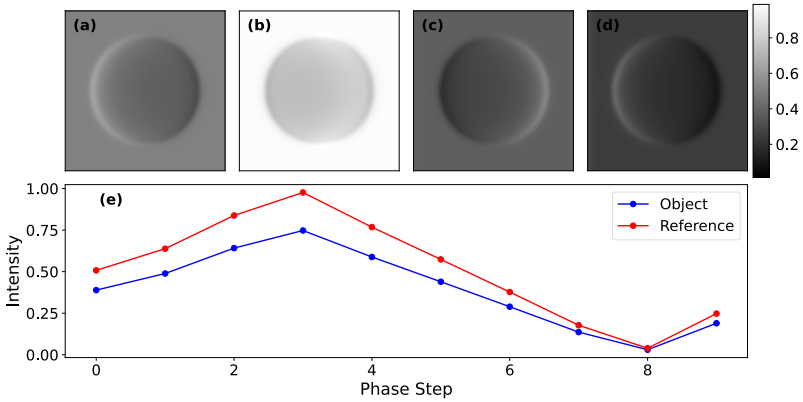

Fig. 11. Talbot-Lau phase contrast images. (a), (b), (c) and (d) consists on the phase steps 0, 3, 6 and 9 respectively. (e) Modulation Intensity Curve for Reference and Object acquisitions for the central pixel.

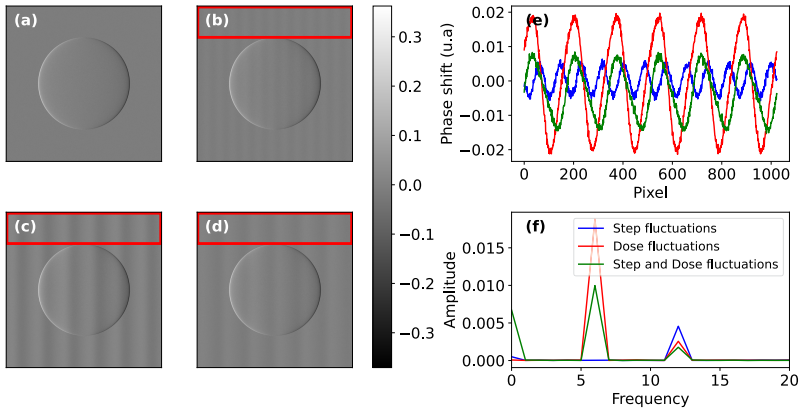

Fig. 12. Differential phase gradient images reconstructed with (a) no fluctuations in the step or dose, (b) fluctuations in the step position, (c) fluctuations in dose, (d) fluctuations in step and dose. (e) Profile averaging the marked rows of (b), (c) and (d). (f) Fourier spectra of (e). Simulations were performed with a pixel size of 1 μm.

3.3. TLRec

To evaluate the experimental feasibility of TLRec, images were acquired using a portable setup that housed the G0, G1, and G2 gratings, as well as the sample and detector (Fig. 14). This robust, steel-constructed desk allows for easy disassembly and repurposing of the X-ray tube for other applications like CT.

Grating details are shown in Fig. 14(a) and (b), with G0 and G2 being 6 μm period gold gratings on silicon, and G1 a 6μm period nickel grating on silicon. The height of nickel is 12.5 μm, corresponding to a phase shift of π at the design energy of 35 keV. The inter-grating distances (z_{01} and z_{12}) were 25 cm. The detector was a flat panel (1246×1650 pixels, 20μm pixel size), yielding an effective 10 μm pixel size with a magnification of 2 due to object placement. Each grating was equipped with a piezoelectric motor for misalignment correction.

An experimental result of a phantom containing a plastic sphere placed on a toothpick, a plastic cylinder, and a nylon fiber, all mounted on a modeling clay base. Experimental conditions included a micro-focus Hamamatsu L10951-04 X-ray tube operating at 60 kV and 600 μA, with

Optics EXPRESS

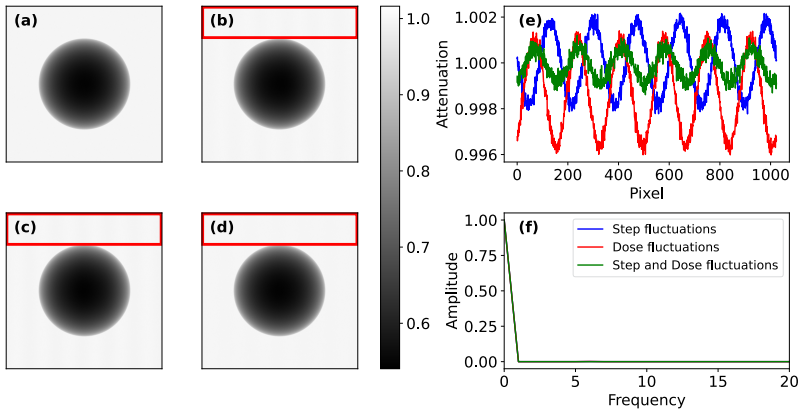

Fig. 13. Attenuation images reconstructed with (a) no fluctuations in the step or dose, (b) fluctuations in the step position, (c) fluctuations in dose, (d) fluctuations in step and dose. (e) Profile averaging the marked rows of (b), (c) and (d). (f) Fourier spectra of (e). Simulations were performed with a pixel size of 1 μm.

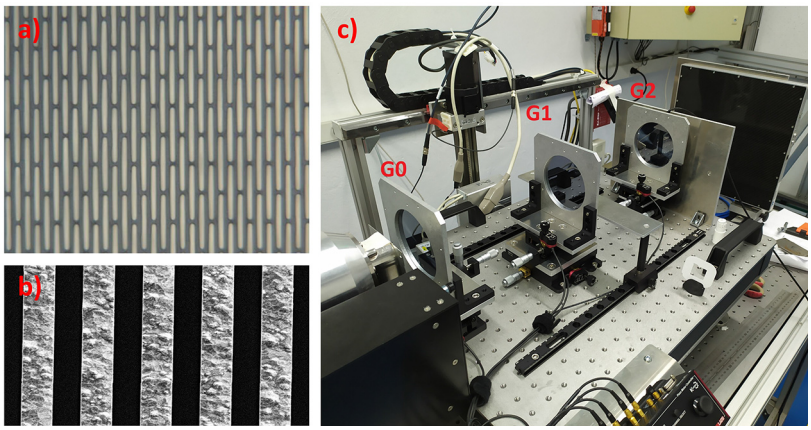

Fig. 14. (a) Absorbption grating (G0 and G2), (b) Phase grating (G1) and (c) Experimental setup used in the acquisition of Talbot-Lau interferometric images.

21 phase steps of 0.3 μm each. This configuration was chosen to achieve a peak energy of 35 keV in G1, which corresponds to the design energy of the system. Figure 15 shows a comparison of object and reference modulation curves for a selected pixel, as well as the stack of phase-stepping images.

The Experimental Retrieval submodule was utilized to reconstruct the phase gradient, attenuation and dark field images (Fig. 16(a)-(c)). The plastic sphere (blue triangle), having higher absorption, exhibits better contrast in the attenuation image (Fig. 16(a)). Conversely, a thin plastic cylinder (green star) shows weak attenuation contrast, and a nylon fiber (red dot) is imperceptible in this image due to low absorption.

The phase gradient image (Fig. 16(b)) demonstrates superior contrast for all phantom objects, including those invisible in the attenuation image, highlighting the utility of phase-contrast imaging. Features like the nylon fiber, plastic sphere, plastic tube, the internal structure of the sphere, and supporting toothpick fibers are clearly visible, as is the plasticine base.

Optics EXPRESS

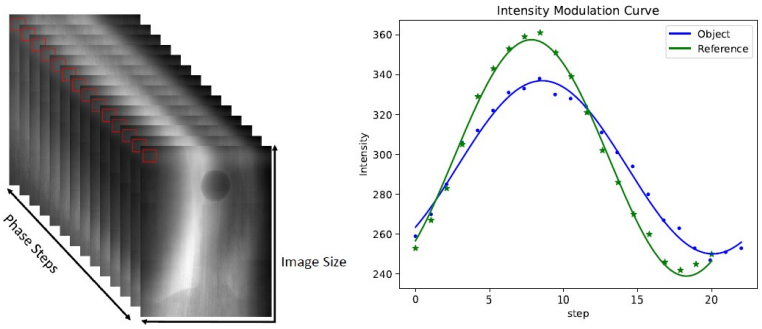

Fig. 15. Left: Stack with all phase stepping images used to retrieve PCI. Right: Intensity modulation curves with an object (blue dots) and without the object (green stars).

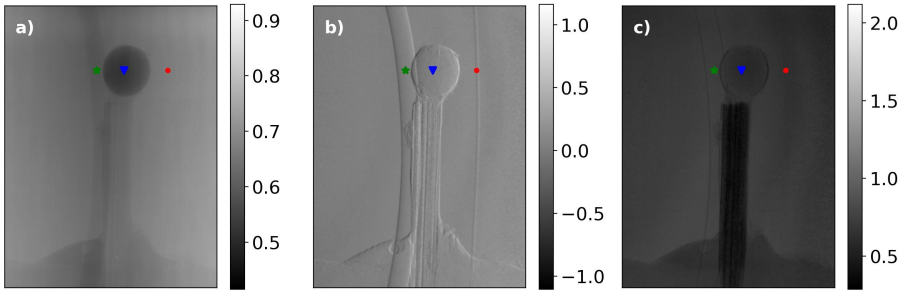

Fig. 16. Results of phase stepping method using the FFT algorithm to retrieve the parameters of the reconstruction. a) Attenuation image, b) Phase Gradient image, c) Dark Field image.

The dark field image (Fig. 16(c)) reveals small-angle scattering from sample inhomogeneities. Edges of the sphere and tube, along with toothpick fibers, yield high contrast in this image, with the toothpick showing the highest contrast due to scattering from its constituent fibers.

Integrated phase images can be obtained by direct integration of the PG or by applying a Wiener filter to smooth local variabilities caused by noise or artifacts (Fig. 17). Direct integration often produces horizontal lines and a continuous phase increase due to noise and Talbot-Lau artifacts. These errors are reduced when using the Wiener filter for integration (Fig. 17(b)).

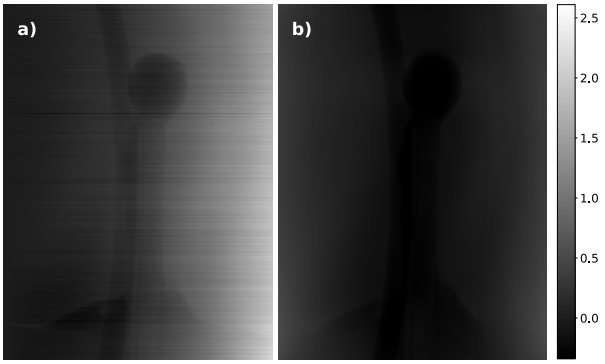

Fig. 17. Integrated phase images obtained using: (a) Direct integration of PG. (b) Application of Wiener filter.

Optics EXPRESS

TLRec also includes an algorithm for retrieving TLPCI images with step fluctuations [28]. Figure 18 compares phase gradient and attenuation images reconstructed using the conventional least squares method and the step fluctuations correction algorithm for the simulation shown in Fig. 12. It is evident that this algorithm reduces artifacts caused by step position fluctuations in both phase gradient and attenuation images. While applied to experimental images (Fig. 19), the Moiré pattern's low signal in these specific images makes the correction less pronounced than in simulations (Fig. 18).

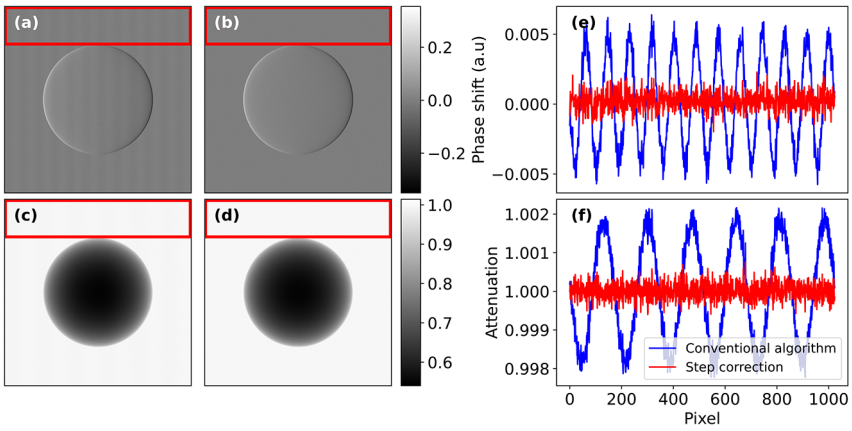

Fig. 18. Simulated Phase Gradient (a-b) and Attenuation (c-d) images obtained using the TLRec algorithm with step correction (b,d) and without step correction (a,c). The mean profiles along the red rectangles in each image are shown in (e) and (f).

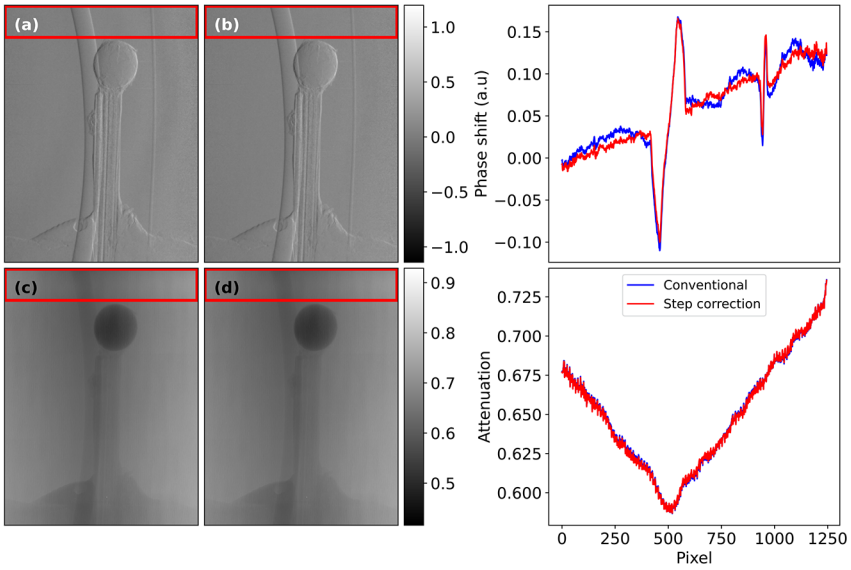

Fig. 19. Experimental Phase Gradient (a-b) and Attenuation (c-d) images obtained using the TLRec algorithm with step correction (b,d) and without step correction (a,c). The mean profiles along the red rectangles in each image are shown in (e) and (f).

Optics EXPRESS

4. Discussion

The developed XPCIpy software provides a versatile and comprehensive framework for X-ray phase-contrast imaging. It enables robust simulations of both PBI and TLPCI images by applying Fresnel's theory of light to X-rays, utilizing simple geometric objects and their complex refractive indices. This simulation capability is crucial for users to model diverse experimental setups and to optimize configurations for enhanced imaging performance.

A significant feature of XPCIpy is its ability to directly compute intensity modulation curves, incorporating various fluctuations to accurately simulate Moiré artifacts. This functionality is particularly valuable for testing advanced algorithms designed to mitigate these patterns in phase-contrast images, or for generating large, varied datasets of Moiré artifacts, which can be essential for training neural networks aimed at artifact reduction [38].

Furthermore, the software's core strength lies in its capability to retrieve phase-contrast images from Talbot-Lau-based acquisitions using the phase stepping method. It incorporates multiple reconstruction algorithms, including those based on fast Fourier transform (FFT) and least squares fitting, offering adaptability to different experimental conditions. Critically, an algorithm for step fluctuation correction, based on a minimization process, is integrated and has been successfully validated, demonstrating its effectiveness in reducing artifacts in both simulated and experimental data, even if less pronounced in some experimental profiles due to low signal Moiré patterns.

By integrating both capabilities within a single tool, XPCIpy significantly streamlines the evaluation of PCI parameters, the optimization of experimental setups, and the rigorous validation of new reconstruction methods. Its modular design is a key advantage, ensuring easy expandability for new functionalities, additional geometric objects, improved detector response models in the simulation module, and the incorporation of novel algorithms in the reconstruction module.

Beyond the individual functionalities, the distinctive contribution of XPCIpy is the integration of simulation and reconstruction within a single, openly accessible framework. This integration provides a practical platform for researchers in the field of phase-contrast imaging, lowering the barrier to explore PCI principles, test different configurations and accessing publicly available reconstruction algorithms without the need to develop their own from scratch.

Future developments for XPCIpy will focus on implementing more advanced phase retrieval algorithms, notably neural network-based reconstruction, and leveraging GPU acceleration to significantly speed up both the simulation and reconstruction processes. Additionally, the current detector model for the simulation presents certain limitations: the point spread functions are modeled using simple Gaussian functions, and the noise model is restricted to basic Gaussian or Poisson distributions. Future improvements may incorporate more realistic PSFs and sophisticated noise models to better replicate actual detector performance, thereby enhancing the overall simulation fidelity.

5. Conclusion

The increasing interest and utility of X-ray phase-contrast imaging (PCI) necessitate robust and accessible tools for its implementation. In this work, we present XPCIpy, a user-friendly, open-source Python platform designed for both the simulation of various PCI modalities and the phase retrieval of images from Talbot-Lau interferometry using the phase-stepping method. XPCIpy's modular architecture facilitates easy integration of new algorithms and functionalities, contributing a valuable open-source framework to the scientific community working in this field. The effectiveness of XPCIpy has been validated through the successful reconstruction of experimental and simulated phase-contrast images. This work demonstrates XPCIpy's value as a versatile and expandable tool for advancing research and applications in X-ray phase-contrast imaging.

Funding. Ministerio de Ciencia, Innovación y Universidades (PID2021-123390OB-C22).

Optics EXPRESS

Acknowledgment. We are grateful to Dr. C. Huerga, Dr. Luis C. Martinez-Gomez and Mr. F.R. Lozano for their insightful discussions, which greatly contributed to this work, as well as for their careful review of the manuscript.

Disclosures. The authors declare the following financial interests which may be considered as potential competing interests: financial support was provided by the Ministry of Science and Innovation of Spain.

Author contribution statement

Victor Sanchez Lara: Conceptualization, Formal analysis, Methodology, Resources, Software, Validation, Visualization, Writing - original draft.

Diego Garcia Pinto: Conceptualization, Methodology, Resources, Project administration, Supervision, Validation, Writing - review and editing.

Data availability. Data underlying the results presented in this paper are publicly available at [39]. The code used for all results is publicly available at [35].

References

1. D. M. Paganin and D. Pelliccia, "Tutorials on X-ray phase contrast imaging: some fundamentals and some conjectures on future developments," (2019).
2. A. Momose, "X-ray phase imaging reaching clinical uses," Physica Medica **79**, 93–102 (2020).
3. G. Giakoumakis, A. Stolidi, and J. Primot, "High resolution x-ray phase contrast imaging for non-destructive testing of composite materials," Research and Review Journal of Nondestructive Testing **2** (2024).
4. E. Castelli, M. Tonutti, F. Arfelli, *et al.*, "Mammography with synchrotron radiation: First clinical experience with phase-detection technique," Radiology **259**(3), 684–694 (2011).
5. S. T. Taba, P. Baran, Y. I. Nesterets, *et al.*, "Comparison of propagation-based ct using synchrotron radiation and conventional cone-beam ct for breast imaging," Eur Radiol **30**(5), 2740–2750 (2020).
6. L. Costello, M. Donnelley, Y. Nesterets, *et al.*, "Evaluating the feasibility of region-of-interest x-ray phase contrast imaging for lung cancer diagnostics," Sci. Rep. **15**(1), 19881 (2025).
7. D. M. Paganin and K. S. Morgan, "X-ray fokker–planck equation for paraxial imaging," Sci. Rep. **9**(1), 17537 (2019).
8. S. Kaeppler, J. Rieger, G. Pelzer, *et al.*, "Improved reconstruction of phase-stepping data for talbot–lau x-ray imaging," J. Med. Imag **4**(03), 1 (2017).
9. N. T. Vo, H. Wang, L. Hu, *et al.*, "Practical implementations of speckle-based phase-retrieval methods in python and gpu for tomography," in *Developments in X–Ray Tomography XIV*, B. Müller and G. Wang, eds. (SPIE, 2022), p. 13–119.
10. O. Oh, D. Kim, H. K. Kim, *et al.*, "Image reconstruction method in grating interferometer with phase stepping using grating position and dose fluctuation correction," J. Instrum. **18**(07), P07006 (2023).
11. A. Momose, S. Kawamoto, I. Koyama, *et al.*, "Demonstration of x-ray talbot interferometry," Jpn. J. Appl. Phys. **42**(Part 2, No. 7B), L866–L868 (2003).
12. D. Paganin, S. C. Mayo, T. E. Gureyev, *et al.*, "Simultaneous phase and amplitude extraction from a single defocused image of a homogeneous object," J. Microsc. **206**(1), 33–40 (2002).
13. M. Langer, P. Cloetens, A. Pacureanu, *et al.*, "X-ray in-line phase tomography of multimaterial objects," Opt. Lett. **37**(11), 2151 (2012).
14. T. E. Gureyev, S. C. Mayo, D. E. Myers, *et al.*, "Refracting röntgen's rays: Propagation-based x-ray phase contrast for biomedical imaging," J. Appl. Phys. **105**(10), 102005 (2009).
15. R. Gradl, M. Dierolf, L. Hehn, *et al.*, "Propagation-based phase-contrast x-ray imaging at a compact light source," Sci. Rep. **7**(1), 4908 (2017).
16. P. Monnin, S. Bulling, J. Hoszowska, *et al.*, "Quantitative characterization of edge enhancement in phase contrast x-ray imaging," Med. Phys. **31**(6), 1372–1383 (2004).
17. L. Weber, A. Hänsch, U. Wolfram, *et al.*, "Registration of phase-contrast images in propagation-based x-ray phase tomography," J. Microsc. **269**(1), 36–47 (2018).
18. S. W. Wilkins, T. E. Gureyev, D. Gao, *et al.*, "Phase-contrast imaging using polychromatic hard x-rays," Nature **384**(6607), 335–338 (1996).
19. R. P. Xian, C. L. Walsh, S. E. Verleden, *et al.*, "A multiscale x-ray phase-contrast tomography dataset of a whole human left lung," Sci. Data **9**(1), 264 (2022).
20. T. Zhou, I. Zanette, M.-C. Zdora, *et al.*, "Speckle-based x-ray phase-contrast imaging with a laboratory source and the scanning technique," Opt. Lett. **40**(12), 2822–2825 (2015).
21. D. Rosich, M. Chevalier, A. Belarra, *et al.*, "Exploring single-shot propagation and speckle based phase recovery techniques for object thickness estimation by using a polychromatic x-ray laboratory source," J. Med. Imag. **11**(04), 043501 (2024).
22. F. Pfeiffer, J. Herzen, M. Willner, *et al.*, "Grating-based x-ray phase contrast for biomedical imaging applications," Z. Med. Phys. **23**(3), 176–185 (2013).
23. F. Pfeiffer, M. Bech, O. Bunk, *et al.*, "X-ray dark-field and phase-contrast imaging using a grating interferometer," J. Appl. Phys. **105**(10), 102006 (2009).
24. T. Thuering and M. Stampanoni, "Performance and optimization of X-ray grating interferometry," Phil. Trans. R. Soc. A. **372**(2010), 20130027 (2014).

Optics EXPRESS

25. T. Weitkamp, A. Diaz, C. David, *et al.*, "X-ray phase imaging with a grating interferometer," Opt. Express **13**(16), 6296 (2005).
26. J. Vila-Comamala, L. Romano, K. Jefimovs, *et al.*, "High sensitivity x-ray phase contrast imaging by laboratory grating-based interferometry at high talbot order geometry," Opt. Express **29**(2), 2049 (2021).
27. C. Hauke, G. Anton, K. Hellbach, *et al.*, "Enhanced reconstruction algorithm for moiréartifact suppression in talbot-lau x-ray imaging," Phys. Med. Biol. **63**(13), 135018 (2018).
28. K. Hashimoto, H. Takano, and A. Momose, "Improved reconstruction method for phase stepping data with stepping errors and dose fluctuations," Opt. Express **28**(11), 16363 (2020).
29. A. Peterzol, J. Berthier, P. Duvauchelle, *et al.*, "X-ray phase contrast image simulation," Nucl. Instrum. Methods Phys. Res., Sect. B **254**(2), 307–318 (2007).
30. V. Arrizón and G. Rojo-Velázquez, "Fractional talbot field of finite gratings: compact analytical formulation," J. Opt. Soc. Am. A **18**(6), 1252 (2001).
31. J. Zeng, J. Huang, J. Zeng, *et al.*, "Restoration of x-ray phase-contrast imaging based on generative adversarial networks," Sci. Rep. **14**(1), 26198 (2024).
32. Y. Xu, S. Tao, Y. Bian, *et al.*, "Single-shot grating-based x-ray phase contrast imaging via generative adversarial network," Optics and Lasers in Engineering **152**, 106960 (2022).
33. N. Bevins, J. Zambelli, K. Li, *et al.*, "Multicontrast x-ray computed tomography imaging using talbot-lau interferometry without phase stepping," Med. Phys. **39**(1), 424–428 (2011).
34. P. Bartl, J. Durst, W. Haas, *et al.*, "Simulation of x-ray phase-contrast imaging using grating-interferometry," in *IEEE Nuclear Science Symposium Conference Record*, (2009), pp.3577–3580.
35. V. Sanchez, "PREDICO-Project / XPCIpy," Github. (2025). https://github.com/PREDICO-Project/XPCIpy
36. D. G. Voelz, *Computational Fourier Optics: A MATLAB Tutorial*, (SPIE, 2011).
37. D. G. Voelz and M. C. Roggemann, "Digital simulation of scalar optical diffraction: revisiting chirp function sampling criteria and consequences," Appl. Opt. **48**(32), 6132 (2009).
38. E. García, D. García-Pinto, V. Sánchez-Lara, *et al.*, "A generative adversarial approach to remove moiré artifacts in dark-field and phase-contrast x-ray images," in *Artificial Intelligence and Imaging for Diagnostic and Treatment Challenges in Breast Care*, R. M. Mann, T. Zhang, T. Tan, *et al.*, eds. (Springer Nature Switzerland, Cham, 2025), pp. 181–190.
39. V. G. Sanchez-Lara and D. Garcia-Pinto, "Talbot Lau Phase Contrast Images," Zenodo, (2025), https://doi.org/10.5281/zenodo.16944391